Supplementary Information for

Fatigue crack-based strain sensors achieving flow detection and motion monitoring for reconnaissance robot applications

Xu-Ping Wu,[ab] Xue-Mei Luo,*[a] Hong-Lei Chen,[a] Yi Man,[ab] Yao-Yao Bai,[c] Tian-Ze Qin,[ab] Bin Zhang,[c] Guang-Ping Zhang*[a]

[a] Shenyang National Laboratory for Materials Science, Institute of Metal Research, Chinese Academy of Sciences, 72 Wenhua Road, Shenyang 110016, China

[b] School of Materials Science and Engineering, University of Science and Technology of China, 72 Wenhua Road, Shenyang 110016, China

[c] Key Laboratory for Anisotropy and Texture of Materials, Ministry of Education, School of Materials Science and Engineering, Northeastern University, 3-11 Wenhua Road, Shenyang 110819, China.

* Corresponding author.

E-mail: xmluo@imr.ac.cn (X.M. Luo), gpzhang@imr.ac.cn (G.P. Zhang)

Experimental section

Preparation of the fatigue crack-based strain sensors: Polyimide has been widely used as the substrate of flexible electronics due to its excellent mechanical properties and chemical stability. Here, we employ polyimide as the substrate of the leaf-like sensor. Au film with prominent chemical stability is used to construct the cracked sensing layer. Firstly, Au films with were deposited on polyimide substrates (Dupont Kapton, 125 μm) by magnetron sputtering with a sputter rate of 0.542 nm/s. The substrate was cleaned by sputtering Ar ions for 5 min before deposition to enhance the interfacial adhesion between the Au film and the polyimide substrate. Then, the as-deposited film was cut into a 2×16 mm rectangle. Copper wires were connected to the two ends of the film by conductive silver adhesive for further electrical characterization. Cracks were introduced to the film through a microforce testing system (SHIMADZU, MMT-101NV-10). For the preparation of pre-fatigue cracks, a tension-tension cyclic loading with a maximum and minimum loading force of 19 N and 1.9 N, respectively, were performed on the film. The loading force generated a peaking strain value of ~2%. The fatigue loading was performed with a periodic sine waveform and a frequency of 30 Hz. After certain cycles of pre-fatigue, the sample stood for ~24 h to release the residual strain in the substrate and thus recover the electrical resistance of the sample. Finally, the fabrication of the flexible strain sensor based on fatigue cracks was completed. For the preparation of pre-tensile cracks, the film was stretched to a strain of 30% with a loading rate of 0.005 mm/s. The other fabrication process of the tensile crack-based sensor was the same as that of the fatigue crack-based sensor.

Assembly of leaf-like mechanosensors: A circular sheet of polyimide (Dupont Kapton, 125 μm) with a diameter of 15 mm was obtained by laser-cutting and then adhered to one end of the rectangular fatigue crack-based strain sensor. The other end of the rectangular sensor was sandwiched by two identical rectangular polyimide sheets for ease of fixing the sensor in different testing scenarios. The length of the bendable cantilever beam was controlled at 7 mm.

Characterization of electromechanical properties: Sensor responses under various loading conditions were investigated on the SHIMAZU microforce testing system. Electrical resistances of the sensor were measured *in situ* by an Agilent 34410 multimeter with a sampling frequency of 10 Hz in a two-point measurement method unless otherwise stated. Tensile responses of the sensor were measured with a loading rate of 0.005 mm/s. Cyclic stability of the sensor was measured with a loading frequency of 1 Hz and a peak strain of 1%. Surface micromorphologies of the fatigue cracks and tensile cracks were characterized by a laser scanning confocal microscope (LSCM, OLS4000) and a scanning electron microscope (SEM, Zeiss Supra 35). In-plane and cross-sectional morphologies of the as-deposited films were characterized by a transmission electron microscope (TEM, FEI Tecnai F20).

Finite element analysis: The Young's modulus of the polyimide substrate is set to be 3.91 GPa according to its stress-strain curves (Fig. S14 in the Supplementary Information). The Poisson's ratio of the substrate is assumed to be 0.35. The bottom of the leaf-like sensor was fixed and a wind pressure was performed vertically on the surface of the leaf-like sensor. The relationship between the wind pressure (p), the flow velocity (v) and the air density ($\rho \approx 1.29$ kg/m^3) can be expressed as follows according to the Bernoulli equation: [S1-S2]

$$p + \frac{1}{2}\rho v^2 + \rho g h = A \tag{1}$$

where A is a constant, ρgh is the gravitational term and is negligible for horizontal flow problems. Therefore, the pressure applied on the surface of the sensor (w) is estimated as:

$$w = p_b - p_f = \frac{1}{2}\rho(v^2 - v_b^2) \approx \frac{1}{2}\rho v^2 \tag{2}$$

where p_f and p_b are the air pressure at the front and the back of the sensor, respectively, v and v_b are the wind velocity at the front and the back of the sensor, respectively, v_b can be estimated to be zero.

Detection of airflow: An electric hairdryer (CONFU, KF-8946) with a working power of 2400 W was used as the wind source. Wind speeds at different testing locations were

tested by a commercial anemometer (Deli, DL333212). For the test of the response and release time of the sensor, the sampling frequency of the Agilent multimeter was set as 200 Hz. The fluctuated original signal under such a high sampling frequency was denoised using a low pass filter on Matlab with a cutoff frequency of 1 Hz. For the detection of the resistance response at different positions, the data was collected continuously. The wind was turn on for ~10 s after the sensor being placed at the designated position. Then, the sensor was carefully moved to the next position after turning off the wind. This operation was repeated until all the nine positions were tested. Since the leaf-like sensor is highly sensitive, an undesirable signal noise is obtained when moving the sensor from one position to another. Therefore, the irregular resistance fluctuation between adjacent testing positions was concealed to make sensor's response to wind more visible. For the detection of wind directions, the wind is turned on and off every time rotating the sensor to a designated direction. The wind source was kept motionless and the distance between the wind source and the sensor was set as 163.5 cm.

Detection of waterflow: The test of waterflow detection was performed in a cubic water tank with a side length of 35 cm. The height of the water level was 15 cm. A water pump with a maximum power of 6 W was attached to an inwall of the water tank to generate waterflow. The leaf-like sensor was fixed on a rod which was connected to a movable crossbeam on the top of the water tank.

Detection of micro-motions of legged robot: The leaf-like sensor was fixed on the back of a quadruped robot (Waveshare, WAVEGO). Movements of the robot were wirelessly controlled by a web page on a mobile phone. Resistance change of the sensor was in situ measured through the Agilent 34410 multimeter with a sampling frequency of 200 Hz. For outdoor recognition of the walking state of the robot, a real-time signal of the sensor was connected through an Arduino Nano board, which was powered by a portable battery (Romoss, PPH10, 10 000 mAh). A user interface was designed to visualize the real-time signals through Labview on a laptop. Wireless interaction between the Arduino board and the user interface was achieved through serial communication with a Bluetooth module (HC-05) integrated into the circuit. The

walking state of the robot was recognized according to the real-time peak-to-peak value of the signal (P). The robot state was recognized as motionless, walking and bumping when $P < 0.02$, $0.02 < P < 0.08$ and $P > 0.08$, respectively.

Supporting Note

Note S1 The influence of sample size on the performance of the leaf-like mechanosensor.

It can be regarded that a force (F) is applied on the center of the baffle disc when the leaf-like sensor is exposed in airflow. Therefore, according to the bending theory of an elastic cantilever beam, the maximum tensile strain (ε) generated on the surface of the leaf-like sensor can be estimated as:

$$\varepsilon = \frac{Fhl}{EI} \tag{3}$$

where h, l, E and I are the sensor thickness, the length of the cantilever beam, elastic modulus of the sensor and the area moment of inertia of the cantilever beam, respectively. The equation (3) indicates that longer l will result in larger ε, which will further lead to higher resistance response of the sensor. Besides, the area moment of inertia can be calculated as:

$$I = \frac{bh^3}{12} \tag{4}$$

where b is the width of the cantilever beam. Therefore, the increasing of the sensor width will cause the increasing of I and then lead to a smaller ε.

Overall, the increasing of sensor length and the decreasing of sensor width is beneficial for enhancing the sensor response. However, structural instability will occur with a large sensor length or a small sensor width. Therefore, a proper ratio between l and d is required for both sensitive sensor response and good structural stability. Research on the optimization of the sensor size can be conducted in the future.

Supporting Table

Table S1 Fitting parameters of fatigue crack-based sensors fabricated through different pre-loading cycles.

Pre-loading cycles	ε_0	μ	C
5×10^5	0.00448	0.83142	45.75760
1×10^6	0.00504	0.62761	30.67902
2×10^6	0.00519	0.78132	88.00182
3×10^6	0.00480	0.78570	93.79158

Supporting Figures

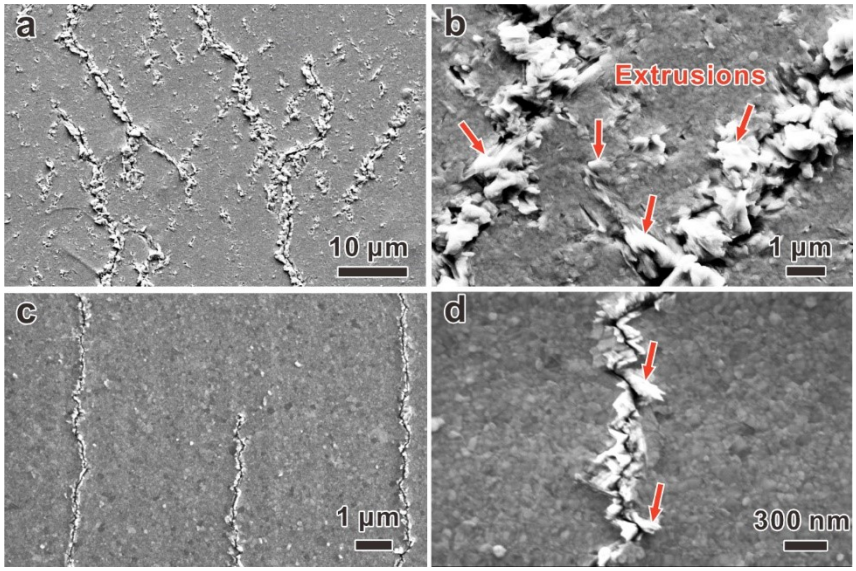

Fig. S1 SEM observations of the surface morphologies of the fatigue cracked Au films with a thickness of (a-b) 930 nm and (c-d) 90 nm.

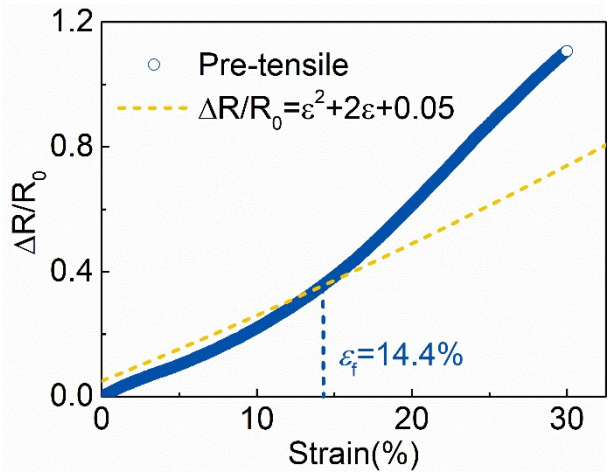

Fig. S2 Electrical resistance of a polyimide-supported gold film as a function of tensile strain. The fracture strain of the film can be determined as the strain where the experimental resistance-strain curve deviates from the theoretical curve by 5%. Therefore, a fracture strain of ε_f=14.4% can be obtained.

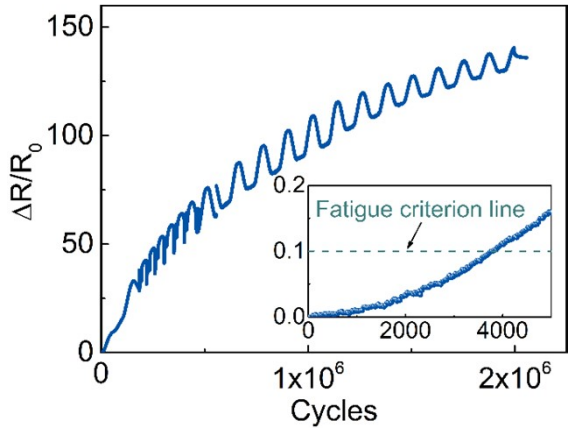

Fig. S3 Resistance variation of the as-fabricated gold film as a function of loading-unloading cycles during the process of pre-fatigue, the inset shows the typical fatigue criterion line, whose intersection with the experimental curve represents the fatigue fracture of the film.

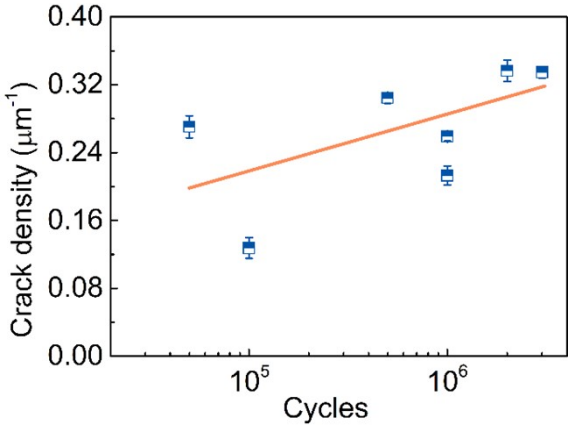

Fig. S4 Crack density as a function of the cycles of pre-fatigue.

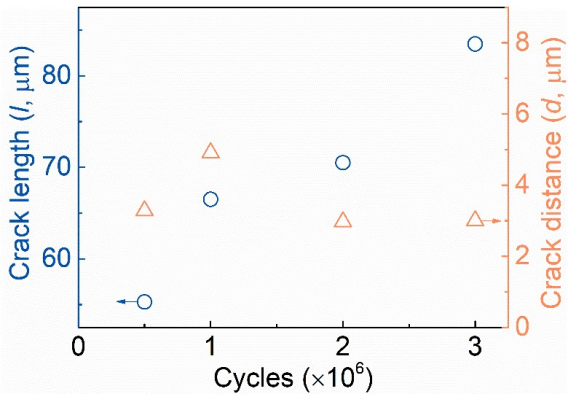

Fig. S5 Averaged length of the fatigue cracks (l) and averaged distance between adjacent cracks (d) as a function of pre-fatigue cycles.

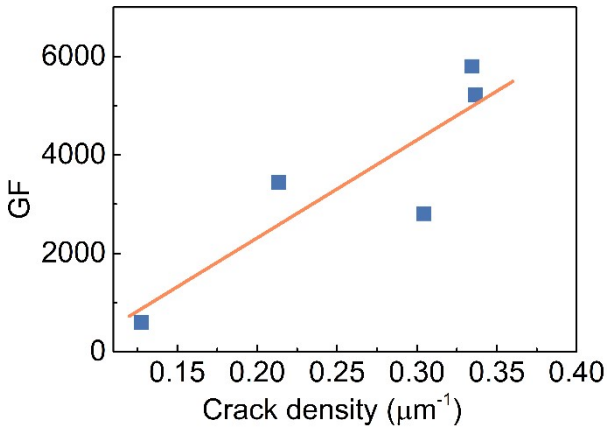

Fig. S6 Gauge factors of the fatigue crack-based sensor as a function of crack density.

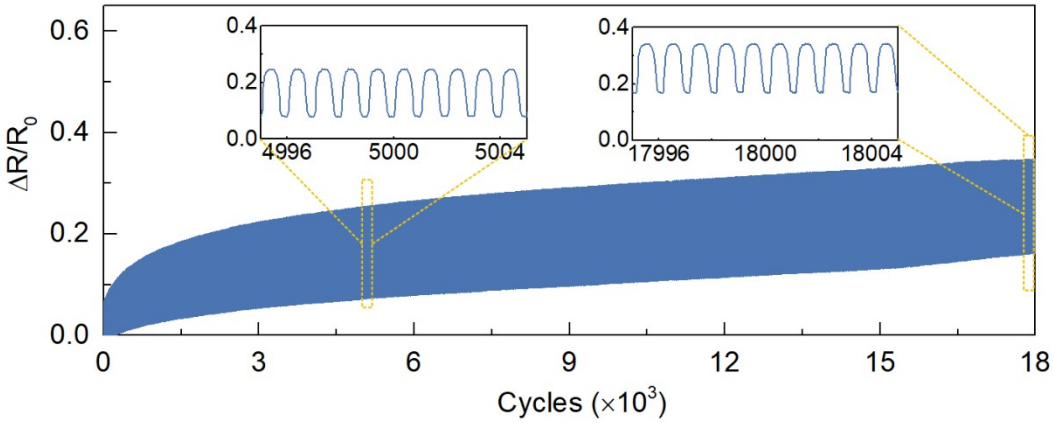

Fig. S7 Cyclic stability of the tensile crack-based sensor. Significant shifts of the cycle maximum value and the cycle minimum value can be observed during the 18000 cycles of loading-unloading test.

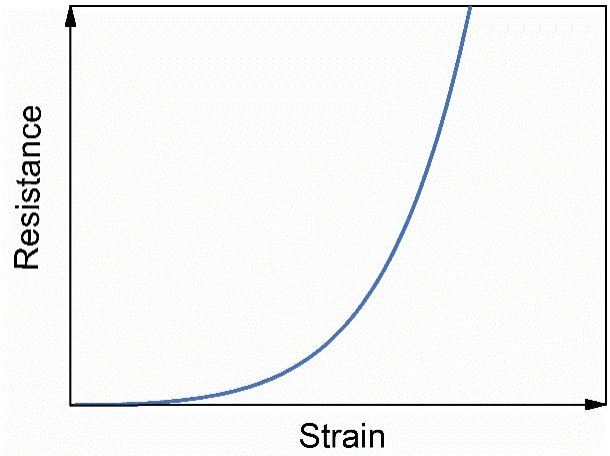

Fig. S8 Typical resistance-strain curve of a channel crack-based strain sensor [S3-S7].

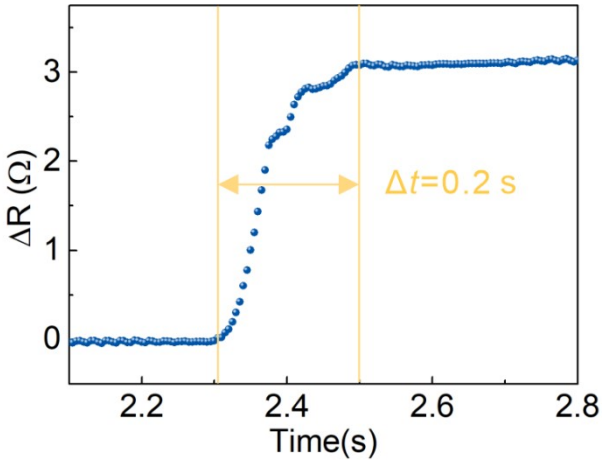

Fig. S9 Response time of the leaf-like sensor measured in a static bending system. The free end of the leaf-like sensor was pressed quasi-transiently to a designated position.

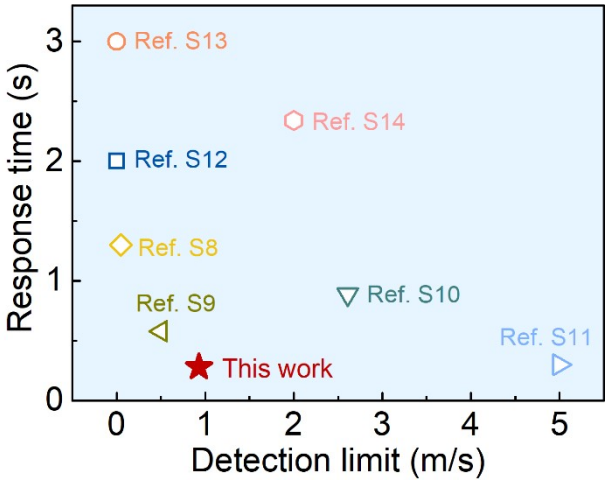

Fig. S10 Sensing performance comparison of the leaf-like mechanosensor with other airflow sensors [S8-S14].

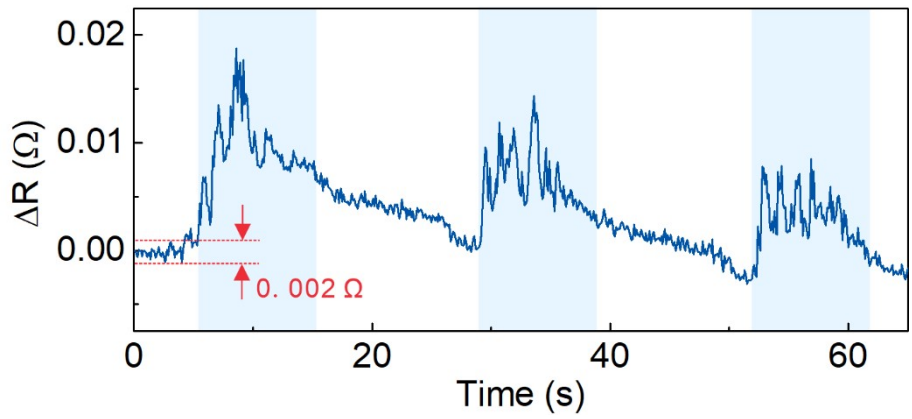

Fig. S11 Resistance response of the sensor under a low wind speed of 0.93 m/s, showing the detection limit of the leaf-like sensor. Here, the detection limit of the leaf-like sensor is the minimum wind speed that can be detected by the sensor with a highly distinguishable signal. The red lines mark that the noise range of the resistance baseline is ~0.002 Ω. The resistance response caused by the airflow is ~0.01 Ω, which is 4 times larger than the noise level. Therefore, the resistance raise caused by the small airflow can be easily recognized and it is concluded that the sensor can detect a wind speed as low as 0.93 m/s.

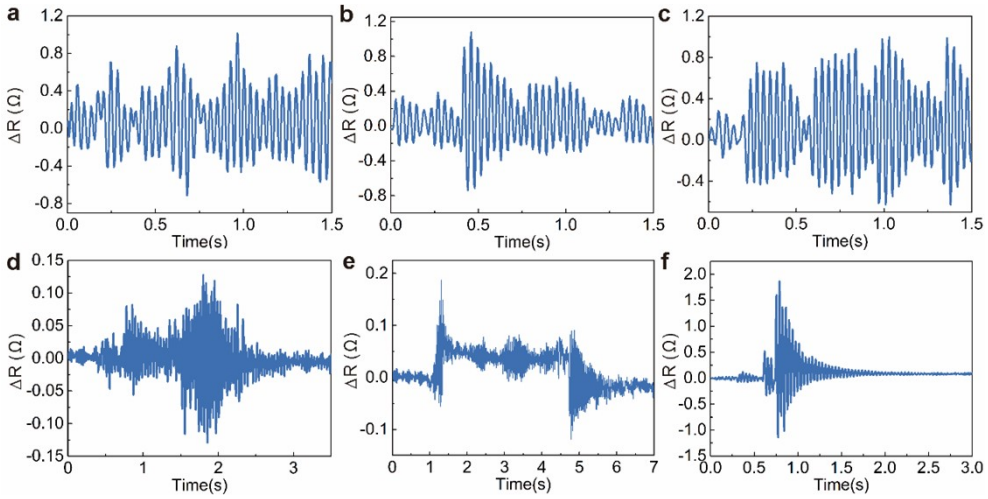

Fig. S12 Detailed resistance responses of a leaf-like sensor that is attached to the back of a quadruped robot when the robot conducts different actions, including **(a)** staying low, **(b)** shaking hand, **(c)** jumping, **(d)** reversing, **(e)** turning left and **(f)** turning right.

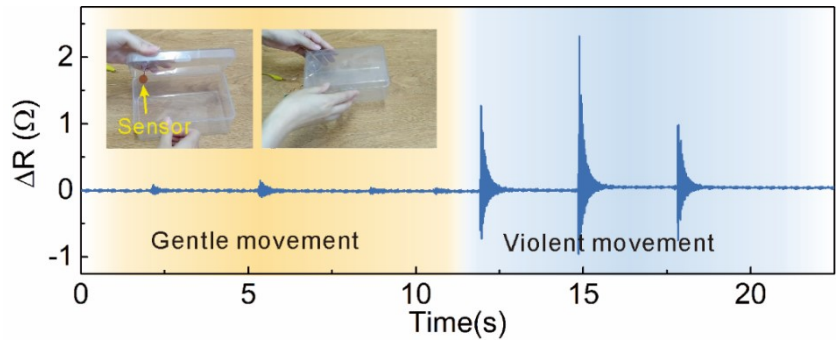

Fig. S13 Resistance response of a leaf-like sensor that is attached to the inwall of a plastic box when the box is moved gently and violently.

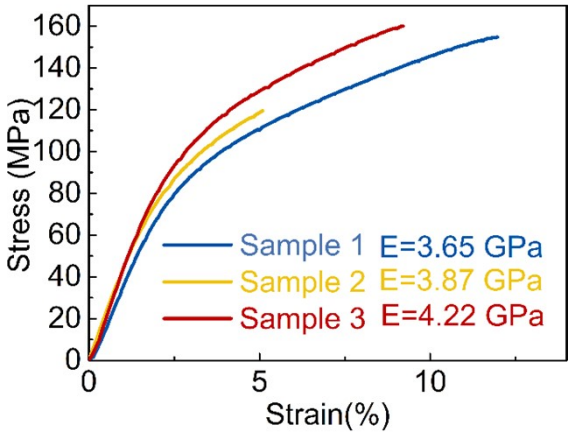

Fig. S14 Stress-strain curves of the gold-coated polyimide substrates with a thickness of 125 μm and a width of 2 mm. The gauge length for tensile test was 10 mm. This curve can be used to estimate the elastic modulus of the polyimide substrate because that the gold film is far thinner than the polyimide substrate. Finally, an average elastic modulus of the polyimide substrate can be calculated to be 3.91 GPa.

Supporting References

S1. H.E. Feustel, M.H. Sherman, A simplified model for predicting air flow in multizone structures. Energy Build. **13**, 217-230 (1989).

S2. R. Qin, C. Duan, The principle and applications of Bernoulli equation. J. Phys. Conf. Ser. **916**, 012038 (2017).

S3. X. Zhao, H. Guo, P. Ding, W. Zhai, C. Liu, et al., Hollow-porous fiber-shaped strain sensor with multiple wrinkle-crack microstructure for strain visualization and wind monitoring. Nano Energy **108**, 108197 (2023).

S4. T. Kim, I. Hong, M. Kim, S. Im, Y. Roh, et al., Ultra-stable and tough bioinspired crack-based tactile sensor for small legged robots. npj Flexible Electron. **7**, 22 (2023).

S5. B. Park, J. Kim, D. Kang, C. Jeong, K.S. Kim, et al., Dramatically enhanced mechanosensitivity and signal-to-noise ratio of nanoscale crack-based sensors: effect of crack depth. Adv. Mater. **28**, 8130-8137 (2016).

S6. D. Kang, P.V. Pikhitsa, Y.W. Choi, C. Lee, S.S. Shin, et al., Ultrasensitive mechanical crack-based sensor inspired by the spider sensory system. Nature **516**, 222-226 (2014).

S7. T.T. Yang, X.M. Li, X. Jiang, S.Y. Lin, J.C. Lao, et al., Structural engineering of gold thin films with channel cracks for ultrasensitive strain sensing. Mater. Horiz. **3**, 248-255 (2016).

S8. H. Wang, S. Li, Y. Wang, H. Wang, X. Shen, et al., Bioinspired fluffy fabric with in situ grown carbon nanotubes for ultrasensitive wearable airflow sensor. Adv. Mater. **32**, 1908214 (2020).

S9. Y. Bian, Y. Zhang, X. Xia, Design and fabrication of a multi-electrode metal-core piezoelectric fiber and its application as an airflow sensor. J. Bionic Eng. **13**, 416-425 (2016).

S10. Y. Bian, R. Liu, S. Hui, Fabrication of a polyvinylidene difluoride fiber with a metal core and its application as directional air flow sensor. Funct. Mater. Lett. **09**, 1650001 (2015).

S11. L. Su, H. Wang, Z. Tian, H. Wang, Q. Cheng, et al., Low detection limit and high sensitivity wind speed sensor based on triboelectrification-induced electroluminescence. Adv. Sci. **6**, 1901980 (2019).

S12. S. Abolpour Moshizi, H. Moradi, S. Wu, Z.J. Han, A. Razmjou, et al., Biomimetic ultraflexible piezoresistive flow sensor based on graphene nanosheets and PVA hydrogel. Adv. Mater. Technol. **7**, 2100783 (2022).

S13. S. Abolpour Moshizi, S. Azadi, A. Belford, A. Razmjou, S. Wu, et al., Development of an ultra-sensitive and flexible piezoresistive flow sensor using vertical graphene nanosheets. Nano-Micro Lett. **12**, 109 (2020).

S14. H. Takahashi, A. Nakai, I. Shimoyama, Waterproof airflow sensor for seabird bio-logging using a highly sensitive differential pressure sensor and nano-hole array. Sensor Actuat. A-Phys. **281**, 243-249 (2018).